Multidisciplinary Materials Chronicles, 2026, Vol. X, Iss. X, 150-165

DOI: 10.62184/mmc.jmmc1100202534

Research Article

SCIENCE PARK PUBLISHER

Multidisciplinary Materials Chronicles

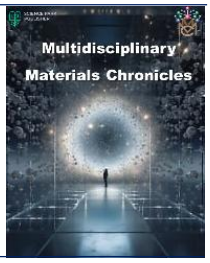

Effect of grain size on the dielectric properties of lanthanum-doped lead titanate perovskite ceramics

Eman N. Serag[1,3], Aseel M. Altarawneh[1,2,*], Osama M. Hemeda[1], S. A. Abdel Gawad[3]

[1] Physics Department, Faculty of Science, Tanta University, 31527 Tanta, Egypt

[2] Ministry of Education, Jordan

[3] Physics Department, Faculty of Engineering, Misr University for Science and Technology, 12649, Egypt

Received: 18, 10, 2025; Accepted: 22, 06, 2026; Published: 19, 07, 2026

Abstract

This study investigates the structural and electrical properties of lanthanum-doped lead titanate, $Pb(La_xTi_{1-\frac{3}{4}x})O_3$, a perovskite-based ceramic material. We used state-of-the-art characterization tools, including scanning electron microscopy (SEM) and X-ray diffraction (XRD), to study how adding lanthanum changed the material's physical properties and microstructure. The results reveal that the dielectric constant (ε) increases with lanthanum content, reaching its maximum at x = 0.06. Electrical conductivity was found to rise with increasing frequency, indicating the dominance of hopping conduction mechanisms. These findings highlight the significant influence of La doping on the dielectric and conductive properties of $PbTiO_3$, demonstrating its potential for advanced electronic applications.

Keywords: Lead titanate; Perovskite; Dipole relaxation; Dielectric constant

1. Introduction

Ferroelectric perovskite oxides have been widely investigated owing to their outstanding dielectric, piezoelectric, and ferroelectric properties, which render them promising candidates for various advanced electronic and multifunctional device applications [1]. These qualities make them very well-suited for use in non-volatile memory devices, transducers, and actuators. The compound known as lead titanate ($PbTiO_3$) has garnered considerable attention among these materials because of its prominent spontaneous polarization and high Curie temperature, which is around 490°C [2]. Pure lead titanium oxide ($PbTiO_2$), on the other hand, has a number of limitations that restrict its practical uses. These shortcomings include poor sinterability, brittleness, a strong coercive field, and thermal instability [3, 4]. For their exceptional dielectric, piezoelectric, electrooptic, electrostrictive, and pyroelectric properties, Lead Lanthanum Titanate (PLT) materials have been extensively investigated for their potential applications in multilayer capacitors, actuators, electro-optical modulators, ultrasonic transducers, and infrared detectors. There is a unique attribute of the PLT that may be improved by adding different ions at the "A" or "B" locations. "Donor" dopants, like La^{+3}, Nb^{+5}, Ce^{+3}, and Ta^{+5}, create "soft" Lead Zirconate Titanate (PZT), whereas "acceptor" dopants, such as Fe^{+3}, create "hard" PZT. Soft dopants improve electrical characteristics over undoped PLT by easing domain wall motion. The integration of La into $PbTiO_3$ results in modifications to the material's physical characteristics, including enhanced permittivity and reduced tetragonality [5, 6].

The use of nanoscale particles in the production of ferroelectric materials has garnered heightened interest in

Multidisciplinary Materials Chronicles, 2026, Vol. X, Iss. X, 150-165

DOI: 10.62184/mmc.jmmc1100202534

Research Article

recent years, since these particles have unique features relative to their bulk equivalents. Diverse synthetic techniques, including hydrothermal approaches such as sol-gel processing and the tartrate precursor technique have been developed to synthesize a diverse array of chemicals at the nanometric scale [1-4]. Lanthanum (La) is one of the most prevalent doping agents in ferroelectric materials, significantly influencing the characteristics of perovskite-structured compounds. Doping at the A-sites of lead titanate leads to a decrease in tetragonality, an enhancement in permittivity and transition temperature (Tc), and a widening of the Curie point temperature [5-9]. The modified materials exhibit a broad spectrum of potential applications across various domains, including dynamic random-access memory, electro-optic systems, and actuator technologies [10-13].

The current work aims to prepare $Pb(La_xTi_{1-\frac{3}{4}x})O_3$ (x = 0, 0.02, 0.04, 0.06, 0.08 and 0.1) nanopowders using tartrate precursor technique and studying the impact of the La^{3+} substitution ratio on the morphology, structure, and ferroelectric characteristics of PLT was examined. It also emphasizes the potential applications of this material in various electrical and optoelectronic devices.

2. Materials and methods

The powders of $Pb(La_xTi_{1-\frac{3}{4}x})O_3$, where x is 0, 0.02, 0.04, 0.06, 0.08 and 0.1, were prepared using the tartrate precursor method. The materials used were titanium dioxide (TiO_2), tartaric acid ($C_4H_6O_6$), lead nitrate ($Pb(NO_3)_2$) with 99% purity, and lanthanum nitrate ($La(NO_3)_3.6H_2O$) with 98% purity. The precise stoichiometric quantities of these chemicals were carefully determined to correspond with the desired La content. The chemicals were weighed in a stoichiometric ratio and mixed with 250 ml of distilled water. The mixture was heated on a magnetic stirrer at 80°C until dry and then dried at 100°C overnight. The powder was collected and annealed at 600°C for 2 hours. It was then pressed into tablets using a compressor at 5MPa. The crystallite size of the prepared samples was measured using X-ray diffraction (XRD) with a Philips model (PW-1729) diffractometer using a wavelength of 1.540598 Å in the 2θ range of (20 to 80°). The morphology of the prepared samples was characterized by the grain size, which was obtained using scanning electron microscope (SEM) with a JEOL model JSM-5600 in the National Research Center, Cairo, Egypt. The grain size was determined from SEM micrographs using the image analysis software *ImageJ*. The SEM images were first calibrated using the scale bar provided in each micrograph. Individual grains were manually outlined, and the equivalent circular diameter was calculated for each grain. A total of N grains (≈ 25–35 grains per sample) were measured to ensure statistical reliability. The average grain size was calculated as the arithmetic mean, and the standard deviation was used to estimate the size dispersion. Grain size distribution histograms were constructed to illustrate the statistical distribution of grain sizes for each sample. The dielectric constant (ε) of the produced samples at various temperatures was measured using an RLC bridge of type BM591 (Solid Lab, Tanta University, Egypt). The weight loss for the prepared ferrite samples was estimated using a thermogravimetric analyzer (TGA-50) with a heating rate of 10°C/min in the range of room temperature to 800°C.

3. Results and discussions

3.1. XRD analysis and discussion

Figure 1 presents the XRD diffraction patterns of $Pb(La_xTi_{1-\frac{3}{4}x})O_3$, which has been subjected to annealing at 600°C for a duration of 2 hours, exhibiting varying La content. The various phases of tetragonal perovskite are observable for La concentrations of x = 0.0, 0.02, 0.04, and 0.06, which correspond to the space group (P4mm).

The perovskite structure is shown by pronounced peaks at 2θ = (21.07°, 31.1°, 38.8°, 49.54°, 55.2°, and 65.49°) for the tetragonal phases. The numbers are (001), (101), (111), (102), (112), and (202). XRD patterns indicate the presence of tetragonal, cubic (predominantly at elevated La concentrations), α-PbO, and rhombohedral phases. The fluctuation in lattice parameters, namely a and c, results from two primary factors: the difference in ionic radii between La and Ti and the simultaneous existence of many contending phases [14, 15].

The Scherrer equation (1) is used to determine the crystallite size (DXRD) from the XRD data of each sample [22].

$$D = \frac{k\lambda}{\beta \cos\theta} \qquad (1)$$

Multidisciplinary Materials Chronicles, 2026, Vol. X, Iss. X, 150-165

DOI: 10.62184/mmc.jmmc1100202534

Research Article

Here, "θ" signifies the location of the diffraction peak, "β" indicates the full width at half maximum (FWHM), and "λ" refers to the X-ray wavelength for Cu-Kα radiation (λ = 1.540598 Å). An observable reduction in crystallite size, as shown in Table 1, occurs with increasing La concentration, reaching a maximum at x = 0.06. The tetragonality factor $\frac{c}{a}$ decreases by increasing La content, except for sample x=0.1 due to the formation of a new phase (α-PbO). Figure 2 shows the La content dependence of the a and c cell parameters and the $\frac{c}{a}$ ratio. The 'a' parameter remains almost constant, whereas the 'c' parameter increases up to 0.06, then decreases. Figure 3 shows that the X-ray density was calculated by using equation (2):

$$\rho_X = \frac{ZM}{N_A V} \qquad (2)$$

M represents the molecular weight, Z denotes the number of molecules per unit cell (Z=1 for the tetragonal phase), N signifies Avogadro's number (N_A=6.022×10²³ mol⁻¹), and V indicates the volume of the unit cell. In Figure 3, we can see the density, which decreases with increasing La content up to 0.06 and then increases for samples with x=0.08 and 0.1. This is related to the higher atomic weights of La (138.9 a.m.u.), Ti (47.9 a.m.u.), and Pb (207 a.m.u.), and to the formation of a cubic phase at x=0.1.

As La^{3+} ions substitute Pb^{2+}, the average A-site ionic radius decreases from 1.49 Å for Pb^{2+} to 1.36 Å for La^{3+}, leading to a slight decrease in the tolerance factor with increasing La concentration.

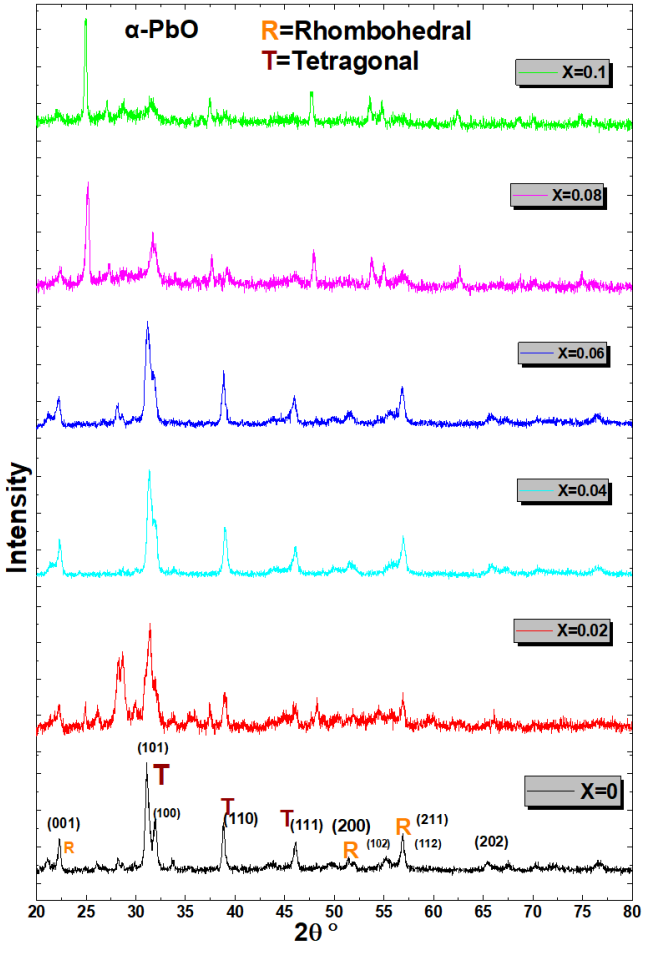

Figure 1. XRD diffraction patterns for $Pb(La_xTi_{1-\frac{3}{4}x})O_3$, where T=tetragonal phases, R=rhombohedral phases and α-PbO phases of [$PLTO_3$].

Multidisciplinary Materials Chronicles, 2026, Vol. X, Iss. X, 150-165

DOI: 10.62184/mmc.jmmc1100202534

Research Article

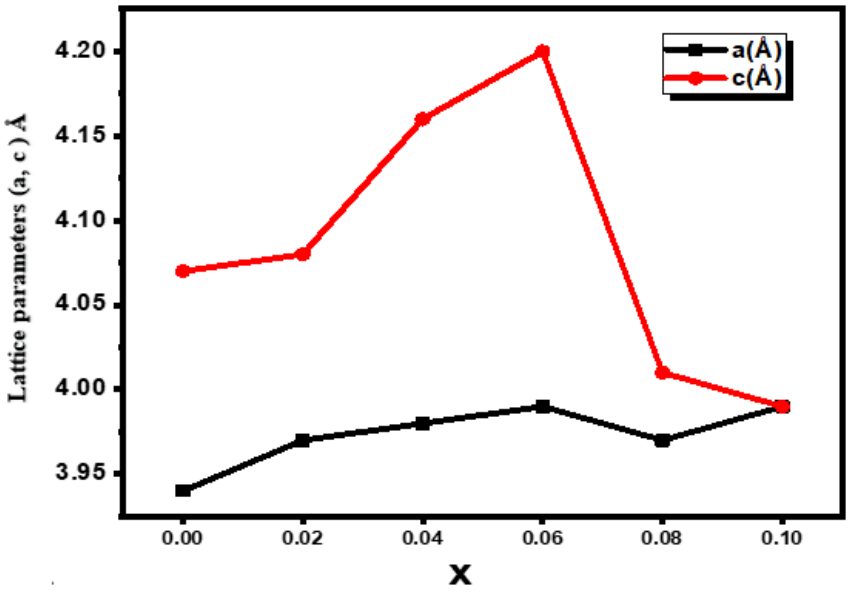

Figure 2. Lattice parameters a and c of the tetragonal phase for Pb($La_xTi_{1-\frac{3}{4}x}$)O_3 samples.

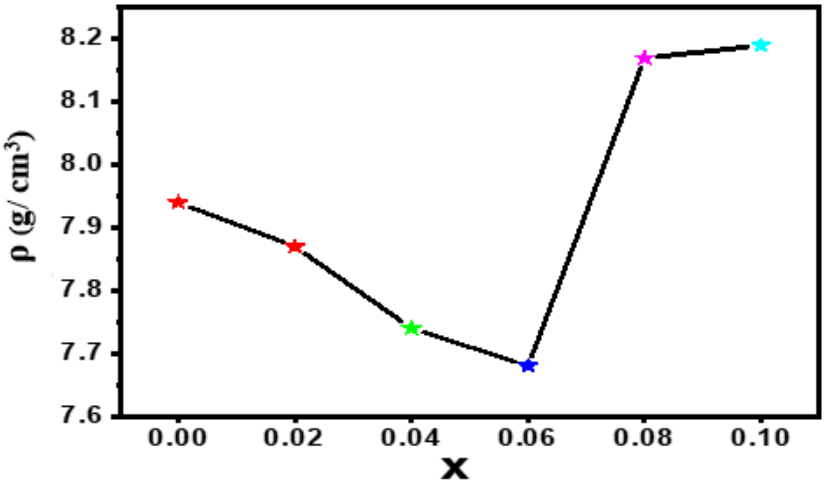

Figure 3. Theoretical density of Pb($La_xTi_{1-\frac{3}{4}x}$)O_3 samples.

3.2. Scanning Electron Microscopy (SEM) micrographs

The morphology of $PbTiO_3$ doped with La ions at various concentrations (x = 0, 0.02, 0.04, 0.06, 0.08, and 0.10) is shown in Figure 4. As listed in Table 1, the grain size ranges from 145 to 277 nm. The decrease in grain size with increasing La content up to x = 0.06 indicates that La ions inhibit grain growth, likely due to lattice distortion and grain boundary pinning effects. For higher La concentrations (x = 0.08 and 0.10), La ions become partially insoluble in the lattice, segregating at grain boundaries or occupying interstitial sites. This results in a slight increase in grain size, which can be attributed to reduced inhibition and coalescence of neighboring grains.

These SEM observations are consistent with the trends obtained from XRD, where crystallite size initially decreases and then slightly increases at higher La concentrations. It is important to note that SEM grain size reflects the physical grains, which may contain multiple crystallites, while XRD crystallite size represents coherent diffraction domains. Thus, the comparison is qualitative, highlighting the influence of La doping on microstructural evolution.

Multidisciplinary Materials Chronicles, 2026, Vol. X, Iss. X, 150-165

DOI: 10.62184/mmc.jmmc1100202534

Research Article

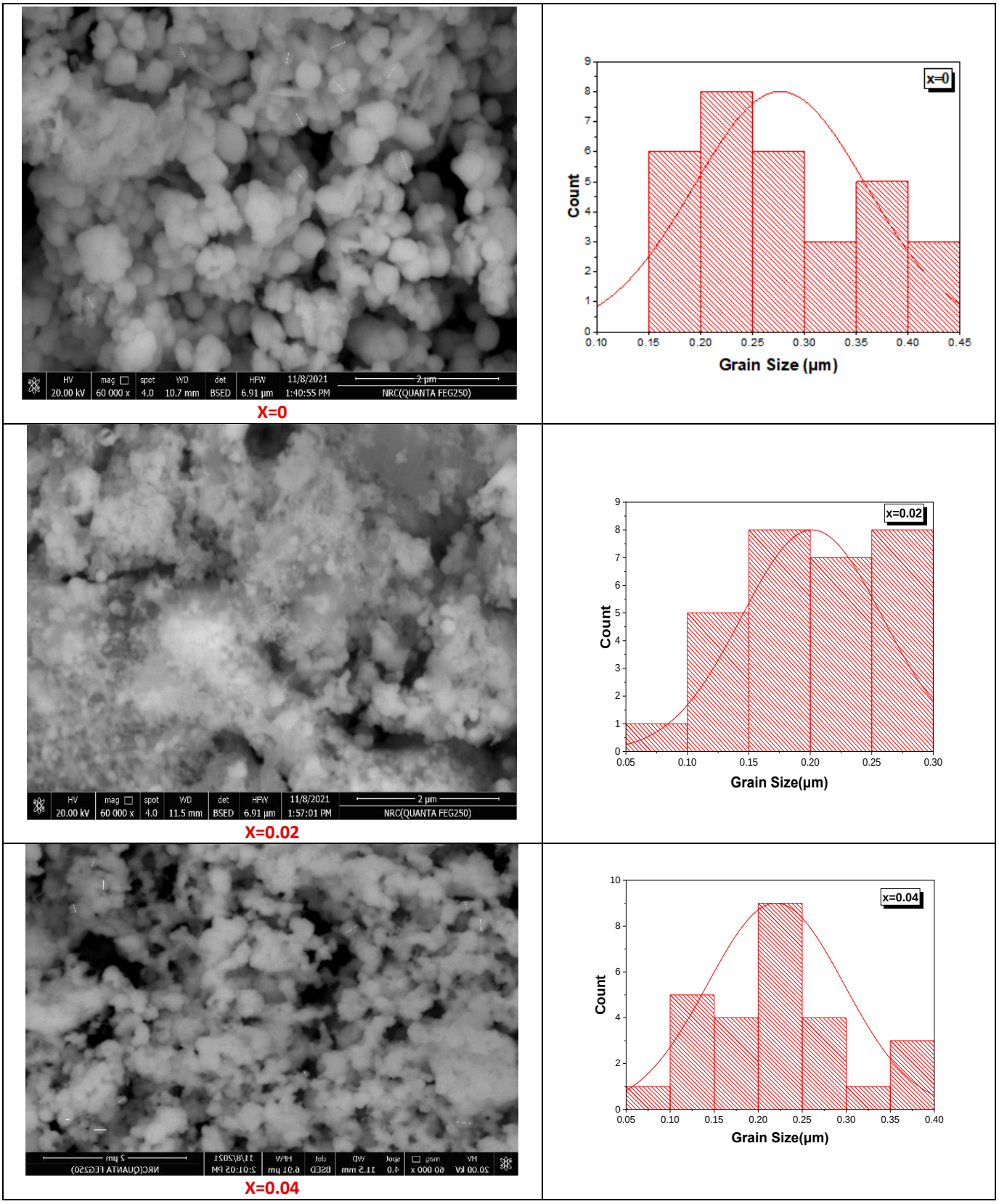

Figure 4. SEM Images along with histogram showing grain size distribution of $Pb(La_xTi_{1-\frac{3}{4}x})O_3$ $(0.00 \leq x \leq 0.1, \Delta x = 0.02)$.

Multidisciplinary Materials Chronicles, 2026, Vol. X, Iss. X, 150-165

DOI: 10.62184/mmc.jmmc1100202534

Research Article

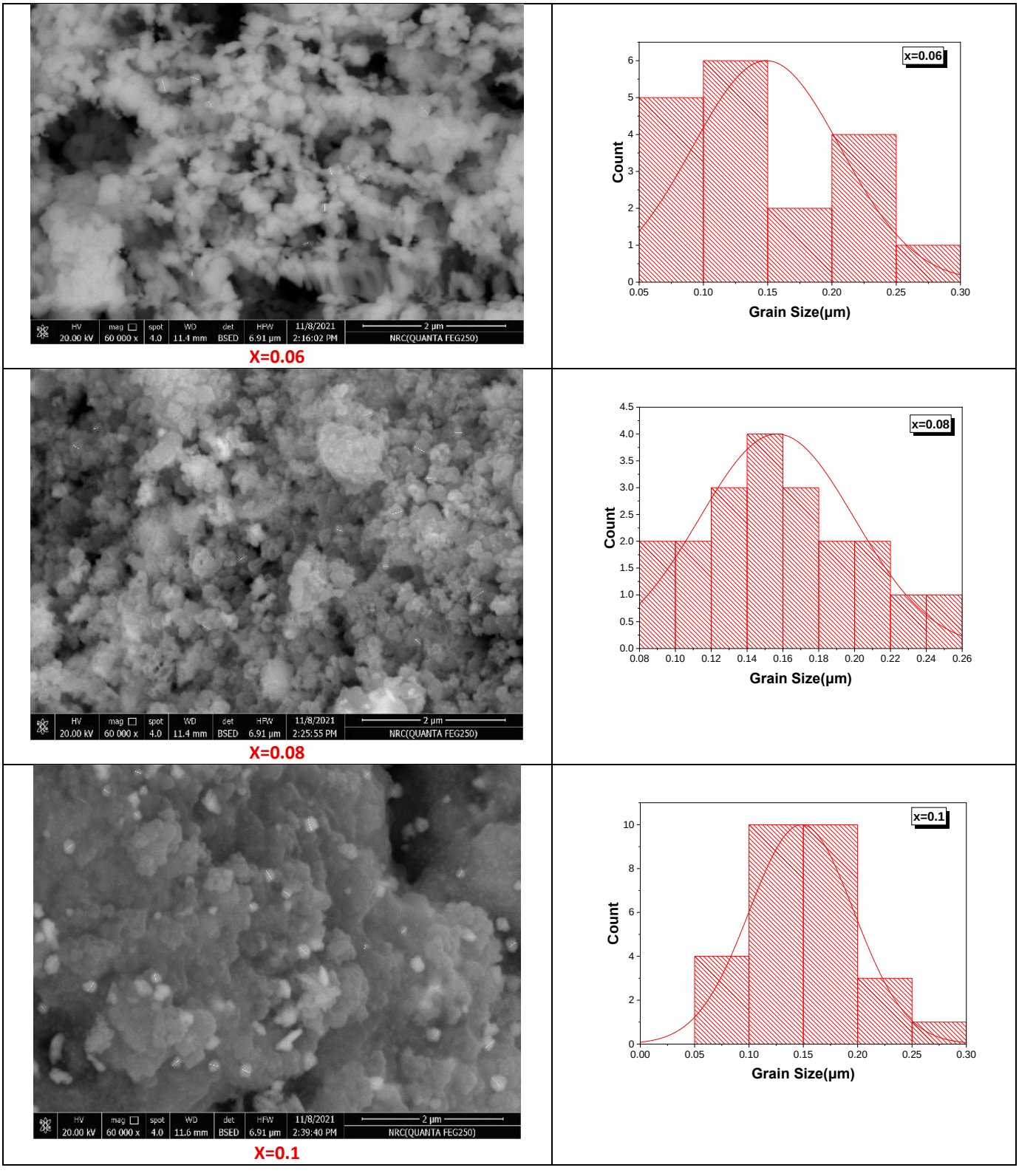

Figure 4. (Continued).

Multidisciplinary Materials Chronicles, 2026, Vol. X, Iss. X, 150-165

DOI: 10.62184/mmc.jmmc1100202534

Research Article

Table 1. The values of crystallite size from XRD and grain size as a function of lanthanum content for Pb($La_xTi_{1-\frac{3}{4}x}$)O_3 samples.

Sample (X)	D (nm) XRD	Grain size (nm) SEM
0.0	24.27	277
0.02	22.02	224
0.04	19.55	202
0.06	17.89	155
0.08	24.76	151
0.1	47.66	145

3.3. Dielectric properties

3.3.1. Dielectric spectroscopy

Figure 5 (a and b) show the variation of the dielectric constant real part (ε′) and its imaginary part (ε′′) as a function of our perovskite sample for different La content. It is clearly seen from the figure that the dielectric constant (ε′ and ε′′) has a high value at low frequency and decreases sharply at high frequency [23, 24]. The hopping electrons between the A-site and B-site are responsible for high polarization at low frequency, leading to a high value of the dielectric constant, whereas at high frequency the electrons are hard to flow the external field frequency, resulting in a decrease of polarization and dielectric constant. At low La content (x = 0.02 and 0.04) the tetragonality of these samples are less than that of the lead titanate sample, leading to a decrease of polarization and dielectric constant. For high La content (x = 0.06 ,0.08 and 0.1), an interfacial polarization is formed due to the interaction of La and $PbTiO_3$, leading to an increase in the polarization and dielectric constant.

Figure 5 (c) illustrates the variation of tan(δ) as a function of frequency, indicating a relaxation peak for samples with elevated La content. The peak identified as the relaxation frequency (F_m) indicates that for frequencies greater than F_m, the charge carriers are confined within their potential well and exhibit short-range movement. On the other hand, the hopping charge carriers are moving over long distances [25, 26]. This material exhibits a transition from long-range to short-range mobility, as indicated by the relaxation frequency derived from equation (3), and is given in Table 2.

$$T_m = \frac{1}{2\pi F_m} \qquad (3)$$

Table 2. Relaxation time (T_m) and frequency (F_m) of Pb($La_xTi_{1-\frac{3}{4}x}$)O_3.

Sample (X)	F_m (Hz)	T_m (Sec) *10^{-3}
0	100	1.59
0.02	14.8	10.78
0.04	21.4	7.44
0.06	94.6	1.68
0.08	170	0.936
0.1	288.4	0.551

Multidisciplinary Materials Chronicles, 2026, Vol. X, Iss. X, 150-165

DOI: 10.62184/mmc.jmmc1100202534

Research Article

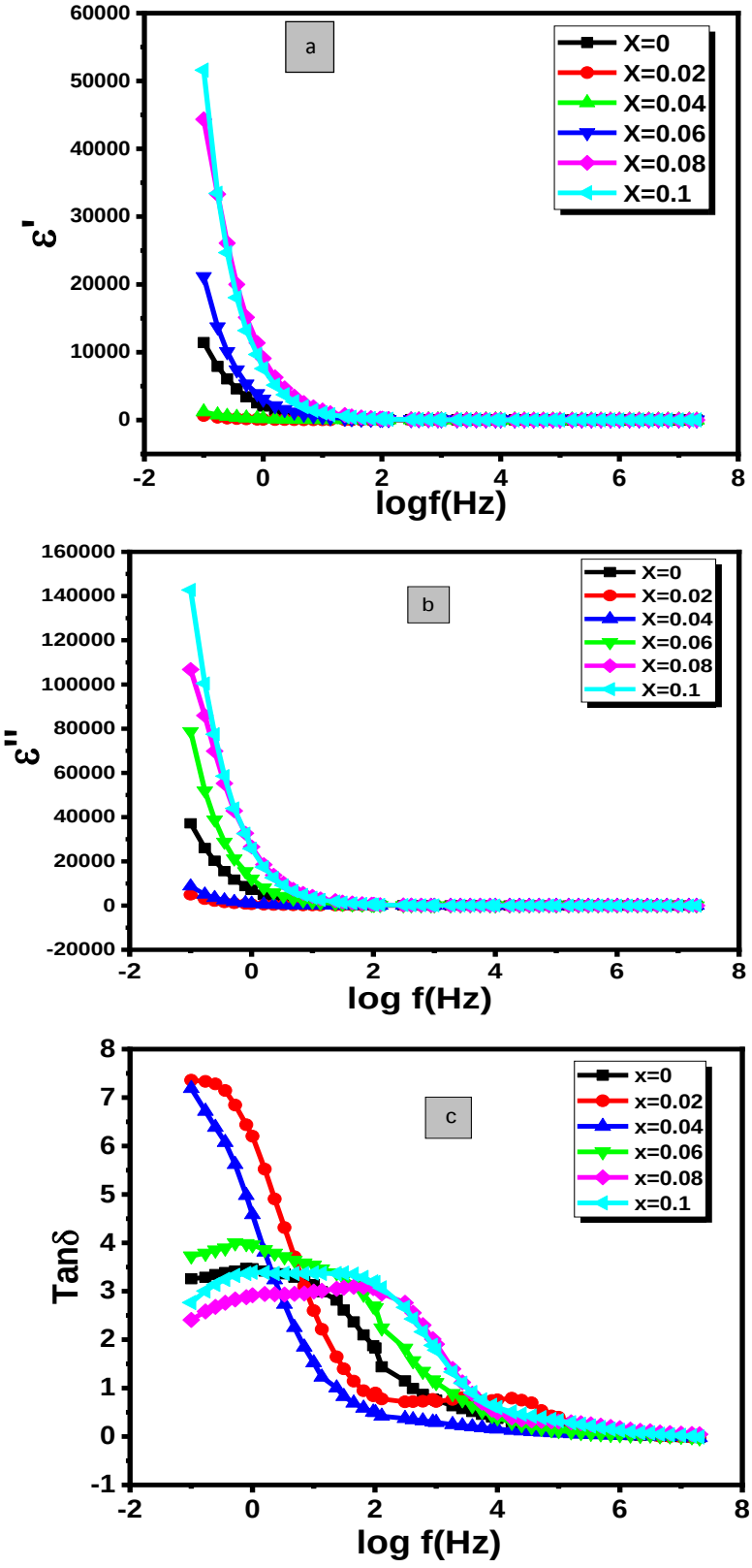

Figure 5. Real and imaginary parts of the dielectric constant and dielectric loss tangent of Pb($La_xTi_{1-\frac{3}{4}x}$)O_3 as a function of frequency.

Multidisciplinary Materials Chronicles, 2026, Vol. X, Iss. X, 150-165

DOI: 10.62184/mmc.jmmc1100202534

Research Article

3.3.2. Electric modulus study

Electric modulus spectra for $PbTiO_3$ doped with La ions are shown in Figure 6 (a and b) as a function of frequency for all La samples. The modulus spectra are useful for understanding of the response of the material, as the electrode polarization effect becomes minimized. The complex electric modulus from equation (4) [27]:

$$M^* = \frac{1}{\varepsilon^*} + (M` + jM``) \qquad (4)$$

where M` and M`` are the real and imaginary part of electrical modulus and ε^* is the complex dielectric constant.

From the figure, it was noticed that at low frequency, the modulus equals zero. up to certain frequency, as given in Table 3, the value for all samples at low frequency is close to zero due to the presence of electrode polarization. After a certain frequency, the modulus begins to increase above the zero value for all samples with La content.

The real part of modulus M` still increases and reaches a maximum at higher frequency because the space charge impact is less. The saturation value is reached at high frequency, suggesting that the electric property of the material is frequency independent [28].

The imaginary part of modulus M`` is shown in Figure 6 (b); at low frequency it has the similar nature of frequency dependance of M`, with the presence of relaxation peak at high frequency which shifts to higher frequency value. The relaxation peak time shifts to lower value by increase La content and was calculated from equation (5):

$$T_m = \frac{1}{2\pi Fm} \qquad (5)$$

The plot of M` and M`` of our samples can be classified as Debye type and non-Debye type as shown in Figure 6 (c), the relaxation is Debye type if the semi-circle is formed with its center line of the real axis (M`) and non-Debye type if the semi-circle is deformed.

In our case, the center of semi-circle is deviated from the M` axis and hence our relaxation process is attributed to a non-Debye type.

The electrical modulus has physical significance in relation to the relaxation mechanism of the electric field, wherein the electric displacement remains constant.

As shown in Table 4, the Cole–Cole plots clearly differentiate the relaxation contributions arising from grains (the more conductive regions) and grain boundaries (the more resistive regions). As shown in Figure 6 (c), the samples with X = 0, 0.02, and 0.06 display a single relaxation peak, indicating that grain boundary effects dominate the conduction mechanism. In contrast, samples with x = 0.04, 0.08, and 0.10 exhibit two relaxation peaks, corresponding to two distinct relaxation times. The first semicircle is attributed to the grain boundary contribution, while the second semicircle arises from the grains themselves [29, 30].

This behavior clearly demonstrates that the observed dielectric relaxation is non-Debye in nature, reflecting the combined influence of grains and grain boundaries on the electrical response of the material. The dielectric relaxation observed in the La-doped $PbTiO_3$ samples exhibits a non-Debye behavior, which is attributed to a distribution of relaxation times rather than a single characteristic time. This is a common feature in polycrystalline materials, where structural heterogeneities such as grain boundaries and defects create multiple relaxation pathways.

Table 3. The relaxation frequency of the real part of electrical modulus for $Pb(La_xTi_{1-\frac{3}{4}x})O_3$.

Sample (X)	F (Hz)
0	100
0.02	94.589
0.04	14.7585
0.06	288.397
0.08	1000
0.1	1848.55

Multidisciplinary Materials Chronicles, 2026, Vol. X, Iss. X, 150-165

DOI: 10.62184/mmc.jmmc1100202534

Research Article

The computed value of the relaxation time is shown in Table 5. The existence of two relaxation peaks in the Cole-Cole diagram (x=0.08 and 0.1) corroborates the presence of two structural phases, as shown by the X-ray pattern of the sample (cubic and tetragonal phases).

3.3.3. Impedance spectroscopy

The dielectric relaxation process in polycrystalline perovskite samples is explained by the impedance spectroscopy, which coincidence as an important to analyze the relationship between the microstructure and electrical properties of the material and can be distinguished by semi-circles and can study the effect of grains, grain boundary and the electrode interface to the electrical properties of the sample [31].

Figure 7 shows the real part (Z`) and imaginary part (Z``) of impedance (Vs) as a function of frequency. The figure shows that Z` is very high at low frequency, then starts to decrease with increasing frequency to reach a constant value and becomes frequency independent at high frequency. The imaginary part of the impedance Z`` has an inverse character to the real part Z`. At low frequency, the grain boundary resistance is high and dominates the grain resistance, which plays an important role at high frequency.

The impedance Z` of the sample with La content (x=0.02 and 0.04) has a higher value than the sample with zero La content, whereas the other samples (x=0.06, 0.08 and 0.1) have a lower Z` value than the sample that is free of La content.

The grain size of both samples (x=0.02 and 0.04) are 170 and 150 nm, respectively, which is greater than the samples (x=0.06, 0.08 and 0.1) as given in Table 6.

Depending on the value of grain size, the grain boundary resistance at low frequency for the abovementioned sample (x=0.02 and 0.04) are greater than the grain boundary resistance for samples (x = 0.06, 0.08 and 0.1), which explains the behavior of real part of impedance for our sample at low frequency [32, 33].

Table 4. The relaxation time and frequency of the imaginary part of electrical modulus for $Pb(La_xTi_{1-\frac{3}{4}x})O_3$.

Sample (X)	F_1 (Hz)	F_2 (Hz)	T_1 (Sec) $*10^{-5}$	T_2 (Sec) $*10^{-5}$
0	5636.52	—	2.825	—
0.02	52377.2	—	0.304	—
0.04	44.9935	606.354	353.9	26.26
0.06	3886.56	—	4.097	—
0.08	5636.52	231534	2.83	0.0688
0.1	8171.5	52377.2	1.95	0.3

Table 5. The relaxation time and frequency for Cole-Cole diagram of $Pb(La_xTi_{1-\frac{3}{4}x})O_3$.

Sample (X)	F_1 (Hz)	F_2 (Hz)	T_1 (Sec) $*10^{-5}$	T_2 (Sec)$*10^{-5}$
0	5636.52	—	2.825	—
0.02	52377.2	—	0.304	—
0.04	65.2406	606.354	244.07	26.26
0.06	3886.56	—	4.097	—
0.08	3886.56	231534	4.097	0.0688
0.1	5636.52	75946.9	2.83	0.209

Multidisciplinary Materials Chronicles, 2026, Vol. X, Iss. X, 150-165

DOI: 10.62184/mmc.jmmc1100202534

Research Article

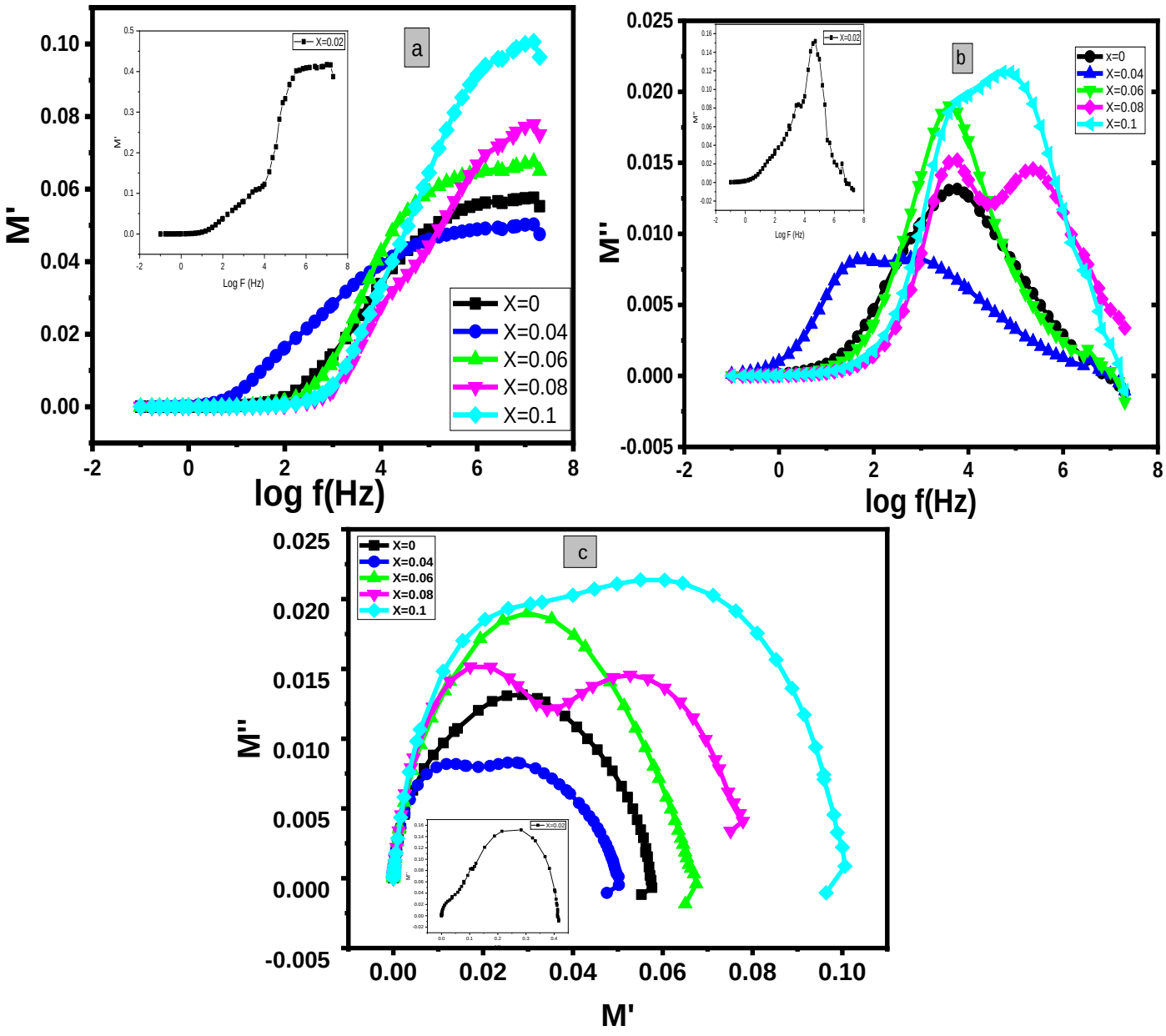

Figure 6. Electric modulus spectra of Pb($La_xTi_{1-\frac{3}{4}x}$)O_3 for different La content as a function of frequency.

Table 6. Impedance (Z`) and grain size of Pb($La_xTi_{1-\frac{3}{4}x}$)O_3.

Sample(X)	Grain size (nm)	Z` at 100Hz
0.02	240.13	$6.84237*10^7$
0.04	147.02	$4.54123*10^7$
0.06	138.36	$1.3254*10^7$
0.08	131.98	$1.3254*10^7$
0.1	116.11	$5.59205*10^7$

Multidisciplinary Materials Chronicles, 2026, Vol. X, Iss. X, 150-165

DOI: 10.62184/mmc.jmmc1100202534

Research Article

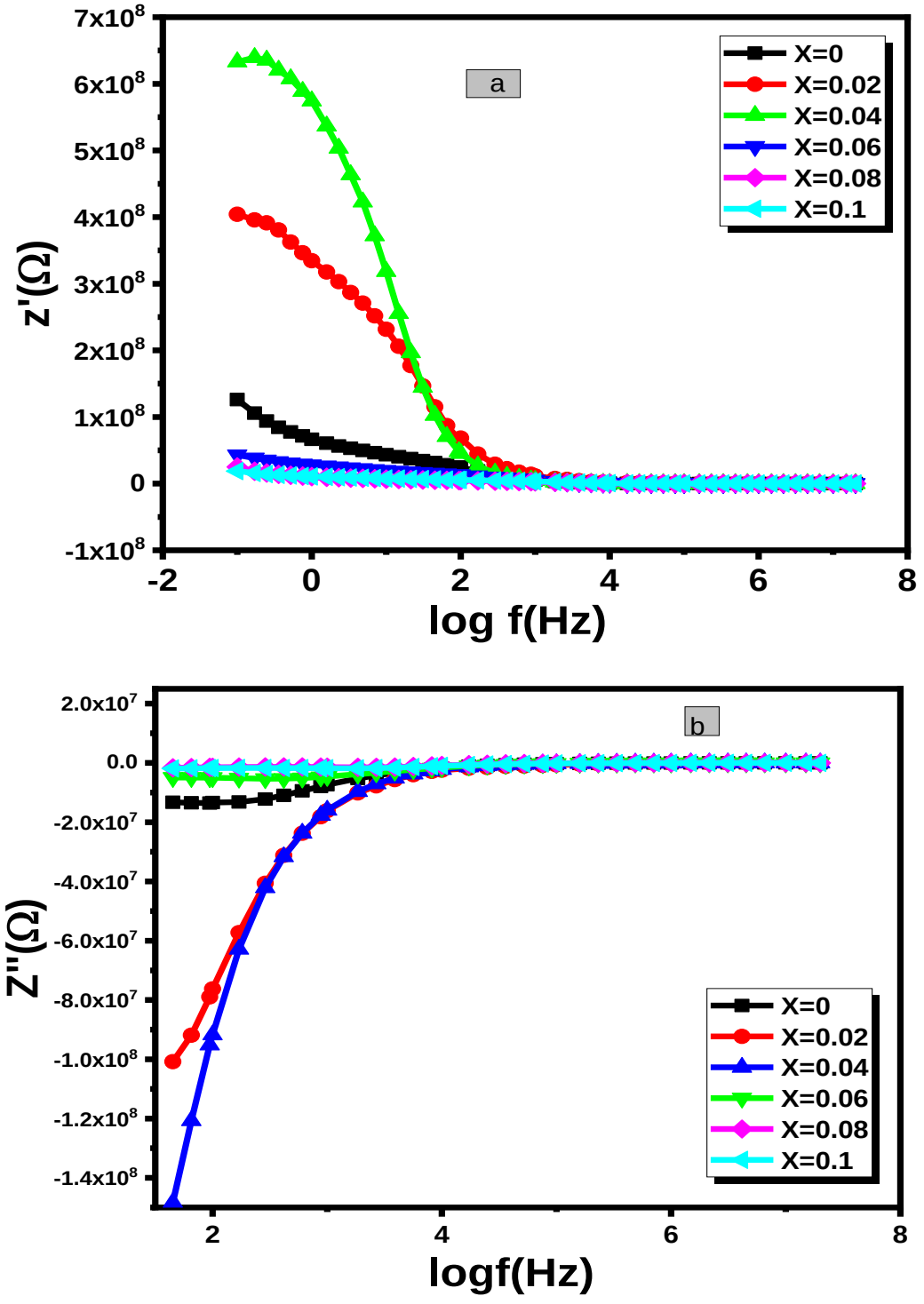

Figure 7. The real part (Z`) and imaginary part (Z") of the impedance of Pb($La_xTi_{1-\frac{3}{4}x}$)O_3 for different La content as a function of frequency.

Multidisciplinary Materials Chronicles, 2026, Vol. X, Iss. X, 150-165

DOI: 10.62184/mmc.jmmc1100202534

Research Article

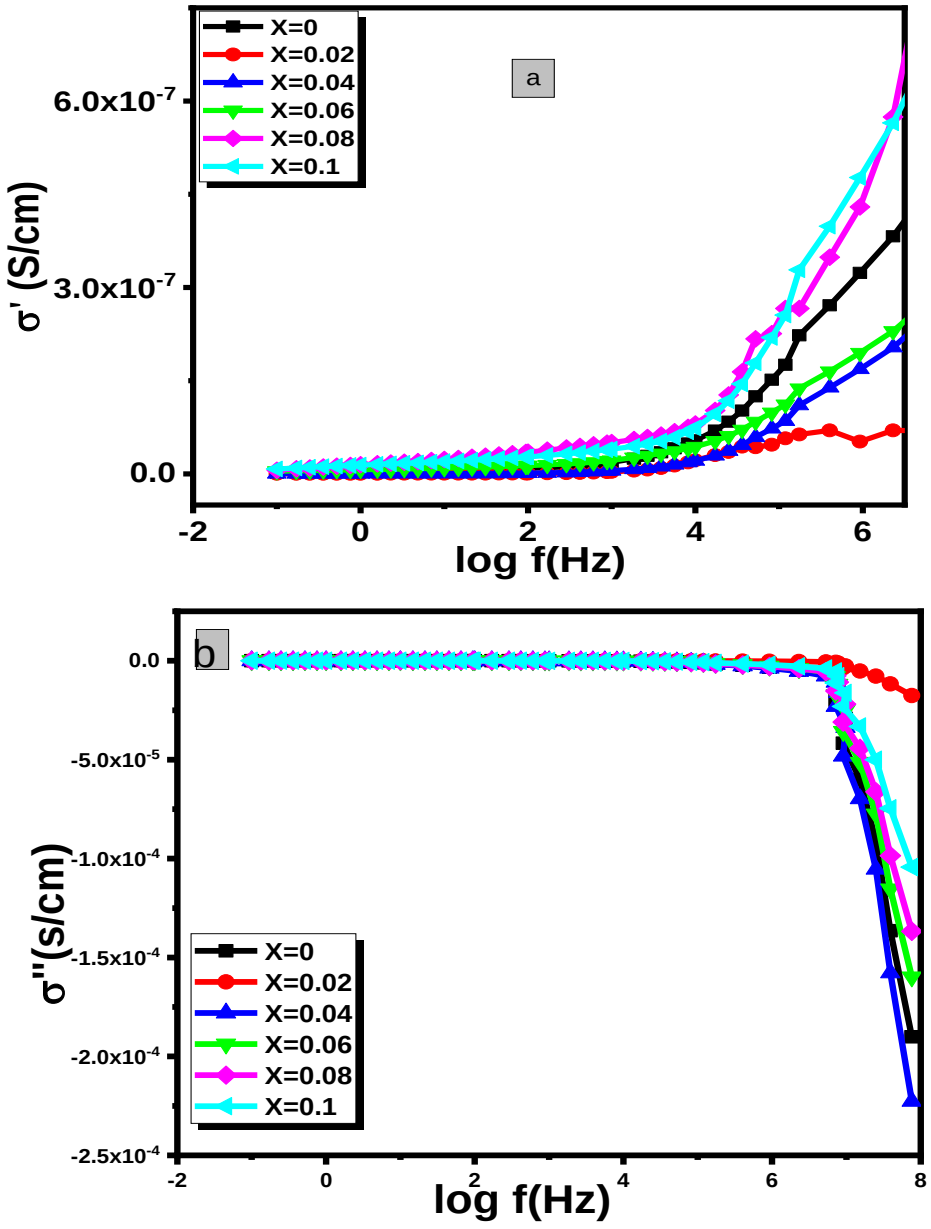

Figure 8. Conductivity σ` and σ`` for the perovskite samples Pb($La_xTi_{1-\frac{3}{4}x}$)O_3 as a function of frequency.

3.3.4. AC conductivity for Pb($La_xTi_{1-\frac{3}{4}x}$)O_3

The variation of σ` and σ`` for the perovskite samples Pb($La_xTi_{1-\frac{3}{4}x}$)O_3 as a function of frequency is shown in Figure 8.

The conductivity exhibits a uniform response at low frequencies and is nearly independent of frequency and La content. The conductivity displays considerable dispersion at higher frequencies [28].

Above a certain frequency, the σ` increases with increasing frequency, which confirms the presence of hopping conduction. σ`` has the same trend as σ` and rebel the same behavior.

DOI: 10.62184/mmc.jmmc1100202534

Research Article

4. Conclusion

In summary, the La doping in $PbTiO_3$ affects the structure, microstructure, and dielectric properties in a correlated manner. XRD analysis shows that doping modifies the crystallite size and lattice parameters, while SEM reveals the corresponding evolution in grain size and morphology. Smaller grains at moderate doping levels (x = 0.02–0.06) result in enhanced grain boundary contributions, which dominate the dielectric relaxation as confirmed by Cole–Cole analysis. At higher doping levels (x = 0.08–0.10), partial solubility of La and grain coalescence lead to increased grain contributions, giving rise to dual relaxation times. This structure–microstructure–property relationship highlights that controlled La doping can tune both the conduction and relaxation behavior of $PbTiO_3$. Based on these findings, the materials exhibit enhanced dielectric and electrical response, making them promising candidates for capacitors, sensors, and microelectronic devices where tailored dielectric relaxation and microstructural control are crucial.

Conflict of interest statement

The authors declare that they have no known competing financial interests or personal relationships that could have appeared to influence the work reported in this paper.

Funding

No funding was received for writing this manuscript.

Authors' contributions

Eman N. Serag: Data collection, analysis.

Aseel M. Altarawneh: Writing – original draft.

Osama M. Hemeda: Discussion data & editing.

S. A. Abdel Gawad: Writing – review**.**

Author information

Corresponding author: Aseel. M. Altarawneh*

E-mail: aseelt682@gmail.com

ORCID iD: 0000-0002-5855-970X

Data availability

Data will be available on request.

References

[1] M. Mesrar, A. Elbasset, N.-S. Echatoui, F. Abdi, T. Lamcharfi, Microstructural and high-temperature dielectric, piezoelectric and complex impedance spectroscopic properties of $K_{0.5}Bi_{0.5}TiO_3$ modified NBT-BT lead-free ferroelectric ceramics, Heliyon 9 (2023) e14761. https://doi.org/10.1016/j.heliyon.2023.e14761.

[2] A. Prasatkhetragarn, T. Sareein, N. Triamnak, R. Yimnirun, Dielectric and ferroelectric properties of modified-$BaTiO_3$ lead-free ceramics prepared by solid solution method, Ferroelectrics 586 (2022) 224–241. https://doi.org/10.1080/00150193.2021.2014274.

[3] M.M. Vijatović, J.D. Bobić, B.D. Stojanović, History and challenges of barium titanate: Part I, Sci. Sinter. 40 (2008) 155–165. https://doi.org/10.2298/sos0803235v.

[4] V.R. Mudinepalli, L. Feng, W.-C. Lin, B.S. Murty, Effect of grain size on dielectric and ferroelectric properties of nanostructured $Ba_{0.8}Sr_{0.2}TiO_3$ ceramics, J. Adv. Ceram. 4 (2015) 46–53. https://doi.org/10.1007/s40145-015-0130-8.

[5] P.P. Neves, A.C. Doriguetto, V.R. Mastelaro, L.P. Lopes, Y.P. Mascarenhas, A. Michalowicz, J.A. Eiras, XAS and XRD structural characterization of lanthanum-modified $PbTiO_3$ ceramic materials, J. Phys. Chem. B. 108 (2004) 14840-14849. https://doi.org/10.1021/jp037166h.

[6] K. Kurihara, M. Kondo, High-strain piezoelectric ceramics and applications to actuators, Ceram. Int. 34 (2008) 695–699. https://doi.org/10.1016/j.ceramint.2007.09.073.

[7] Z. Yu, C. Ang, Electrical and magnetic properties of $BaTiO_3$-$(Ni_{0.3}Zn_{0.7})Fe_{2.1}O_4$ composites, J. Mater. Sci.: Mater. Electron. 13 (2002) 193-196. https://doi.org/10.1023/a:1014819731557.

[8] S.R. Wadgane, S.T. Alone, A. Karim, G. Vats, S.E. Shirsath, R.H. Kadam, Magnetic field induced polarization and magnetoelectric effect in $Na_{0.5}Bi_{0.5}TiO_3$–$Co_{0.75}Zn_{0.25}Cr_{0.2}Fe_{1.8}O_4$ multiferroic composite, J. Magn. Magn. Mater. 471 (2019) 388–393. https://doi.org/10.1016/j.jmmm.2018.10.011.

[9] N.H.J. Jamil, I. Izzuddin, Z. Zainuddin, M.H.H. Jumali, Microstructural studies of nanocrystalline barium zirconium titanate (BZT) for piezoelectric applications, AIP Conf. Proc. 1678 (2015) 040008. https://doi.org/10.1063/1.4931265.

[10] C.W. Nan, M.I. Bichurin, S. Dong, D. Viehland, G. Srinivasan, Multiferroic magnetoelectric composites: Historical perspective, status, and future directions, J. Appl. Phys. 103 (2008) 031101. https://doi.org/10.1063/1.2836410.

DOI: 10.62184/mmc.jmmc1100202534

Research Article

[11] R. Bujakiewicz-Koronska, Ł. Gondek, L. Vasylechko, M. Balanda, E. Juszynska-Galazka, Magnetoelectric, spectroscopic, optical and elastic properties of Co-doped $BaTiO_3$ ceramics, J. Alloys Compd. 946 (2023) 169344. https://doi.org/10.1016/j.jallcom.2023.169344.

[12] G. Shirane, E. Sawaguchi, Y Takagi, Dielectric properties of lead zirconate, Phys. Rev. 84 (1951) 476–481. https://doi.org/10.1103/PhysRev.84.476.

[13] Y. Yafet, C. Kittel, Antiferromagnetic arrangements in ferrites. Phys. Rev. 87 (1952) 290-294. https://doi.org/10.1103/PhysRev.87.290.

[14] Z. Liu, H. Wu, J. Zhuang, G. Niu, N. Zhang, W. Ren, Z. G. Ye, High Curie temperature bismuth-based piezo-/ferroelectric single crystals of complex perovskite structure: Recent progress and perspectives, Cryst. Eng. Comm. 24 (2022) 220–230. https://doi.org/10.1039/d1ce00962a.

[15] O.M. Hemeda, A. Tawfik, A.M. Dorgham, M.A. Hamad, The effect of Zr content on the thermal stability, dielectric and pyroelectric behavior for lead zirconate prepared by tartrate precursor method, Appl. Phys. A: Mater. Sci. Process. 125 (2019) 370-376. https://doi.org/10.1007/s00339-019-2666-x.

[16] S.L. Swartz, Topics in electronic ceramics. IEEE Trans. Electr. Insul. 25 (1990) 935–987. https://doi.org/10.1109/14.59868.

[17] S.K. Rout, Phase Formation and Dielectric Studies of Some BaO-TiO_2-ZrO_2 Based Perovskite System (Thesis), National Institute of Technology, Rourkela, 2006.

[18] E. Aksel, J.L. Jones, Advances in lead-free piezoelectric materials for sensors and actuators, Sensors 10 (2010) 1935–1954. https://doi.org/10.3390/s100301935.

[19] M.A.Darwish, M.M. Salem, H.M.H. Zakaly, W. Abd-Elaziem, M.M. Abou Halaka, M.S. Eid, E.N. Serag, M.K. Hossain, O.M. Hemeda, H.M. Badran, A. Elmekawy, Perovskite ceramics: The impact of lanthanum doping on the structural, radiation shielding and vibrational characteristics of lead titanate, Appl. Phys. A: Mater. Sci. Process. 130 (2024) 348. https://doi.org/10.1007/s00339-024-07485-9.

[20] M. Salem, E.N. Serag, O.M. Hemeda, A.M. Altarawneh, A.M.A. Henaish, S.A. Abdelgawad, Investigating the structural and dielectric properties of La-doped $PbLa_xTi_{(1-3/4x)}O_3$ perovskite ceramics: The role of La content, Delta J. Sci. 46 (2023) 58–68. https://doi.org/10.21608/djs.2023.187668.1073.

[21] A. Aslam, A. Razzaq, S. Naz, N. Amin, M.I. Arshad, M.A.U. Nabi, A. Nawaz, K. Mahmood, A. Bibi, F. Iqbal, M. Shakil, Z. Farooq, M.Z. Iqbal, S. Haider, A.U. Rehman, Impact of lanthanum-doping on the physical and electrical properties of cobalt ferrites, J. Supercond. Nov. Magn. 34 (2021) 1855–1864. https://doi.org/10.1007/s10948-021-05802-4.

[22] R.S. Devan, S.B. Deshpande, B.K. Chougule, Ferroelectric and ferromagnetic properties of (x)$BaTiO_3$ + (1-x)$Ni_{0.94}Co_{0.01}Cu_{0.05}Fe_2O_4$ composite, J. Phys. D: Appl. Phys. 40 (2007) 1864–1868. https://doi.org/10.1088/0022-3727/40/7/004.

[23] M. Abba, A. Boutarfaia, Z. Necira, N. Abdessalem, H. Menasra, A. Meklid, Investigation on the microstructure and electrical properties of the compositionally modified PZT ceramics prepared by mixed-oxide method, MSA. 4 (2013) 723–729. http://dx.doi.org/10.4236/msa.2013.411091.

[24] C. Rayssi, S.E. Kossi, J. Dhahri, K. Khirouni, Frequency and temperature-dependence of dielectric permittivity and electric modulus studies of the solid solution $Ca_{0.85}Er_{0.1}Ti_{1-x}Co_{4x/3}O_3$ ($0 \leq x \leq 0.1$), RSC Adv. 8 (2018) 17139–17150. https://doi.org/10.1039/c8ra00794b.

[25] A. Tachafine, D. Fasquelle, R. Desfeux, A. Ferri, A.D. Costa, J.C. Carru, A. Outzourhit, Doping effect on nanoscopic and macroscopic electrical properties of barium zirconate titanate thin films, Spectrosc. Lett. 54 (2021) 507–519. https://doi.org/10.1080/00387010.2021.1928223.

[26] R. Mumtaz, W.H. Shah, Y. Iqbal, H. Ullah, G. Asghar, M. Hussain, M. R. Abukhadra, A.M. El-Sherbeeny, Electrical transport and dielectric relaxation mechanism in $Zn_{0.5}Cd_{0.5}Fe_2O_4$ spinel ferrite: A temperature- and frequency-dependent complex impedance study, Heliyon 10 (2024) e34155. https://doi.org/10.1016/j.heliyon.2024.e34155.

[27] F.I.H. Rhouma, A. Dhahri, J. Dhahri, M.A. Valente, Dielectric, modulus and impedance analysis of lead-free ceramics $Ba_{0.8}La_{0.133}Ti_{1-x}Sn_xO_3$ (x = 0.15 and 0.2), Appl. Phys. A: Mater. Sci. Process. 108. (2012) 593–600. https://doi.org/10.1007/s00339-012-6935-1.

[28] M. Hashim, Alimuddin, S. Kumar, S. Ali, B.H. Koo, H. Chung, R. Kumar, Structural, magnetic and electrical

DOI: 10.62184/mmc.jmmc1100202534

properties of Al^{3+} substituted Ni-Zn ferrite nanoparticles, J. Alloys Compd. 511 (2012) 107–114. https://doi.org/10.1016/j.jallcom.2011.08.096.

[29] S.T. Assar, H.F. Abosheiasha, M.K. El Nimr, Study of the dielectric behavior of Co-Ni-Li nanoferrites, J. Magn. Magn. Mater. 350 (2014) 12–18. https://doi.org/10.1016/j.jmmm.2013.09.022.

[30] D.S. Saini, S. Tripathy, A. Kumar, S.K. Sharma, A. Ghosh, D. Bhattacharya, Impedance and modulus spectroscopic analysis of single phase $BaZrO_3$ ceramics for SOFC application. Ionics 24 (2018) 1161–1171. https://doi.org/10.1007/s11581-017-2282-8.

[31] S. Hcini, S. Khadhraoui, A. Triki, S. Zemni, M. Boudard, M. Oumezzine, Impedance spectroscopy properties of $Pr_{0.67}A_{0.33}MnO_3$ (A = Ba or Sr) perovskites, J. Supercond. Nov. Magn. 27 (2014) 195–201. https://doi.org/10.1007/s10948-013-2240-2.

[32] M.V. Petrović, J. Bobić, R. Grigalaitis, B. Stojanović, J. Banys, La-doped and La/Mn-co-doped barium titanate ceramics, Acta Phys. Pol. B. 124 (2013) 155–160. https://doi.org/10.12693/aphyspola.124.155.